CrossMark

ORIGINAL RESEARCH

Synthesis optimization of carbon-supported ZrO$_2$ nanoparticles from different organometallic precursors

Pankaj Madkikar[1] · Xiaodong Wang[2] · Thomas Mittermeier[1] ·
Alessandro H. A. Monteverde Videla[3] · Christoph Denk[1] · Stefania Specchia[3] ·
Hubert A. Gasteiger[1] · Michele Piana[1]

Abstract We report here the synthesis of carbon-supported ZrO$_2$ nanoparticles from zirconium oxyphthalocyanine (ZrOPc) and acetylacetonate [Zr(acac)$_4$]. Using thermogravimetric analysis (TGA) coupled with mass spectrometry (MS), we could investigate the thermal decomposition behavior of the chosen precursors. According to those results, we chose the heat treatment temperatures (T_{HT}) using partial oxidizing (PO) and reducing (RED) atmosphere. By X-ray diffraction we detected structure and size of the nanoparticles; the size was further confirmed by transmission electron microscopy. ZrO$_2$ formation happens at lower temperature with Zr(acac)$_4$ than with ZrOPc, due to the lower thermal stability and a higher oxygen amount in Zr(acac)$_4$. Using ZrOPc at $T_{HT} \geq 900$ °C, PO conditions facilitate the crystallite growth and formation of distinct tetragonal ZrO$_2$, while with Zr(acac)$_4$ a distinct tetragonal ZrO$_2$ phase is observed already at $T_{HT} \geq 750$ °C in both RED and PO conditions. Tuning of ZrO$_2$ nanocrystallite size from 5 to 9 nm by varying the precursor loading is also demonstrated. The chemical state of zirconium was analyzed by X-ray photoelectron spectroscopy, which confirms ZrO$_2$ formation from different synthesis routes.

Introduction

Bulk zirconia has been explored over decades. ZrO$_2$ exists in three phases, viz., monoclinic (a room temperature stable phase), tetragonal (stable above 1100 °C), and cubic (stable above 2300 °C); the latter two are thus called high-temperature phases [1]. Various mechanisms are reported which explain the stabilization of high-temperature ZrO$_2$ phases at room temperature [2, 3]. ZrO$_2$ stabilized with dopants like yttria, magnesia, and alumina has a wide range of applications in solid-oxide fuel cells, thermal barrier coatings, and biomedical implants [4–6]. In comparison to the work done on bulk ZrO$_2$, carbon-supported ZrO$_2$ nanoparticles are not much explored. Recently, works on the applications of carbon-supported ZrO$_2$ nanoparticles were reported. Sulfated ZrO$_2$ supported on multiwalled carbon nanotubes (MWCNTs) as a support for platinum is an example; the resulting catalyst is claimed to exhibit a higher methanol oxidation reaction (MOR) activity than unsulfated Pt-ZrO$_2$/MWCNT and commercial Pt/C [7]. Sulfated-ZrO$_2$ acts as a co-catalyst of Pt, resulting in could be a relatively cheap anode catalyst in comparison to PtRu for MOR. Another example of application are ZrO$_2$-C hybrid supports for Pt electrocatalysts to increase the stability of noble metal during the course of potential cycling [8]. Here it is reported, that the increase in durability is due to nanometric ZrO$_2$

✉ Pankaj Madkikar
pankaj.madkikar@tum.de

[1] Chair of Technical Electrochemistry, Department of Chemistry and Catalysis Research Center, Technische Universität München, 85748 Garching, Germany

[2] Johnson Matthey Catalysts (Germany) GmbH, Bahnhofstr. 43, 96257 Redwitz, Germany

[3] Department of Applied Science and Technology, Politecnico di Torino, Corso Duca degli Abruzzi 24, 10129 Turin, Italy

which inhibits the migration and aggregation of Pt during cycling. Similar ZrO_2-C hybrid supports for Pd catalysts are reported to show higher activity and durability than Pd/C in formic acid electro-oxidation [9]. In the latter study, the authors concluded that the physical characteristics of ZrO_2 could promote dispersion of Pd nanoparticles and the presence of ZrO_2 could change the interaction of Pd with the support material, resulting in increased activity and reduced CO poisoning effect on Pd. There were also several other articles published which clearly indicated that ZrO_2 serves as co-catalyst in energy conversion [10–13]. In 2013, Seo et al. reported the synthesis of valve-metal-oxide nanoparticles by an electrodeposition technique as oxygen-reduction-reaction (ORR) electrocatalysts [14]. Sebastián et al. have also reported facile synthesis of Zr- and Ta-based ORR-active methanol-tolerant catalysts for direct alcohol fuel cells (DAFCs) [15]. In addition, Ota research group has also reported ORR activity for ZrO_2 [16, 17]. This material has been considered as a promising non-noble metal catalyst for PEMFCs (proton exchange membrane fuel cells) because of its availability, its observed ORR activity, and stability in the strong acidic environment of the PEMFC [18]. In a few conference proceedings articles, zirconium oxy-phthalocyanine (ZrOPc) has been used as a starting precursor for ZrO_2 nanoparticles synthesis [19–21], however, lacking detailed information and study of that synthesis. Carbon-supported ZrO_2 is not restricted to only DAFCs and PEMFCs applications; it has also used as a cathode in microbial fuel cell (MFC) as reported by Mecheri et al. [22].

Looking into this growing interest in carbon-supported valve-metal oxide nanoparticles like zirconia and lacking the scientific detailed information on its synthesis using ZrOPc as a precursor, this work provides a study on the preparation of ZrO_2 nanoparticles under different conditions. Two precursors, zirconium oxyphthalocyanine (ZrOPc) and zirconium acetylacetonate [$Zr(acac)_4$], were chosen based on previous studies [19, 23] especially for their difference in atomic constitutions and solubility in organic solvents. ZrOPc contains less molecular oxygen but is nitrogen-rich, while, $Zr(acac)_4$ is an oxygen-rich but nitrogen-free precursor. Furthermore, ZrOPc is barely soluble in common organic solvents like chloroform, acetone, ethanol, etc., in contrast to $Zr(acac)_4$, which is soluble [24, 25]. Starting from these highly different precursors, we aimed at comparing the structure, size, and ORR activity of the resulting carbon supported ZrO_2 nanoparticles.

The organometallic precursors were first supported on carbon. The obtained precursor was heat-treated at different temperatures ranging from 350 to 1000 °C, using two different gas conditions, i.e., reducing (RED) (5% H_2 in Ar) or partially oxidizing (PO) (0.5% O_2 in 2.5% H_2 in a mixture of N_2 and Ar). Additionally, ZrO_2 loading variation was also carried out by varying the starting amount of ZrOPc and its

effect on the oxide nanoparticles was checked. Our final aim was to check the ORR activity of the supported nanoparticles and find a possible correlation between their activity and size–structure. We have reported the electrochemical results in an electrochemistry-oriented journal [26].

Experimental procedure

Synthesis of carbon supported ZrO_2 nanoparticles

Zirconium oxy-phthalocyanine (ZrOPc) was synthesized as reported by Tomachynski et al. (Refer to the supplementary information for the chemical analyses of the produced ZrOPc) [27]. Zirconium acetylacetonate [$Zr(acac)_4$, 98%] and chloroform ($CHCl_3$, ≥99.9%) were purchased from Sigma-Aldrich. Ketjenblack E-type (KB) carbon support was bought from Tanaka Kikinzoku Kogyo K.K. Argon 5.0 (Ar, 99.999%), hydrogen W5 (5% H_2 in Ar), and synthetic air (a mixture of 20.5% O_2 and 79.5% N_2) were supplied by Westfalen AG. All the commercial chemicals and gases were used as received without further purification.

For the synthesis of carbon-supported ZrO_2 nanoparticles, initially the precursors were deposited on KB by a method developed on the similar guidelines described in US 2011/0034325 A1 patent [28]. The general scheme is depicted in Fig. 1. Typically, 504 mg of ZrOPc (Zr = 0.8 mmol) or 220 mg of $Zr(acac)_4$ (Zr = 0.45 mmol) were added to 200 ml $CHCl_3$ in a 500 ml round-bottom flask. Considering different precursor losses in two different $CHCl_3$ separation methods for both precursors, the initial Zr mmoles are different to obtain similar Zr-loadings after supporting on carbon. The mixture was then sonicated for 5 min in an ice-cold ultrasonic bath. After this a uniform dispersion/solution was formed, which was dark blue colored in the case of ZrOPc and colorless in $Zr(acac)_4$. Thereafter, 403 mg of KB and an additional 200 ml of $CHCl_3$ were added to the flask. Ice-cold bath sonication was continued for another 2.5 h and the dispersion was observed to be uniform. To ensure the maximum deposition of ZrOPc or $Zr(acac)_4$ on the carbon support, the sonicated dispersion was further kept under continuous stirring at 20 °C for 48 h. Afterwards, the carbon-supported precursor was isolated from $CHCl_3$ by centrifugation (*Eppendorf, Centrifuge 5810 R*) in the case of ZrOPc/KB and by rotovaporation (*Heidolph, Hei-VAP Value*) in the case $Zr(acac)_4$/KB. The collected residue was dried at RT, then ground to fine powder in a mortar with pestle, and further dried in a temperature controlled vacuum oven at 70 °C overnight, to ensure complete removal of $CHCl_3$.

Thermogravimetric analysis (TGA) of both ZrOPc/KB and $Zr(acac)_4$/KB was performed on a *Mettler Toledo TGA/DSC 1* instrument to check the thermal stability and

Fig. 1 Scheme of the steps and conditions involved in the synthesis of supported ZrO_2 nanoparticles

degradation pattern of the precursors in both Ar and H_2/Ar atmospheres, adopting a heating rate of 20 °C/min in the analysis. In addition, TGA-MS analysis of unsupported ZrOPc and $Zr(acac)_4$ was carried out with *Pfeiffer Vacuum Thermostar* mass spectrometer (MS) in Ar atmosphere with a heating rate of 10 °C/min to obtain the fragmentation pattern of the precursors. Unsupported organometallic precursors were used in MS analysis to avoid signals from carbon, which might overlap with the signals from molecular fragments and cause possible complications in the data interpretation.

From the TGA of the carbon supported precursors (see discussion of Figs. 2, 5) we chose the desired gas conditions (PO or RED) and temperatures (350–1000 °C) for the final heat treatment in a quartz tube furnace (*HTM Reetz*). PO conditions were selected to be similar to those reported by Yin et al. [20].

In the above depositions of ZrOPc and $Zr(acac)_4$ on KB, the targeted ZrO_2 loading on carbon was 13 wt.% ZrO_2/KB for both. Additionally, a loading variation study was conducted with carbon supported ZrOPc, to investigate its effect on the resulting particle size and structure. Samples with three loadings of ZrO_2 on KB, i.e., 5, 10, and 15 wt.%, were synthesized by varying the relative amount of ZrOPc with respect to KB during the supporting process and heat-treating in PO conditions at 950 °C.

Size–structural characterization of supported ZrO_2 nanoparticles

All heat-treated samples were analyzed by a *STOE* X-ray powder diffractometer (XRD), equipped with molybdenum (Mo) Kα1 ($\lambda = 0.7093$ Å, 50 kV, 40 mA) X-ray source and a one-dimensional silicon strip detector Mythen 1 K (*Dectris*). The measurements were conducted in a Debye–Scherrer geometry with a 2θ range of 2°–50° and a step size of 0.015° 2θ. Crystallite sizes were determined using the Scherrer equation on the (111) reflection (13.6°– 13.8° 2θ), correcting the values for instrumental broadening. Transmission electron microscopy (TEM) measurements were conducted on the samples to evaluate their particle size and distribution. The measurements were performed with a *JEOL JEM 2010* transmission electronic microscope equipped with a tungsten cathode, operated at an acceleration voltage of 120 kV. Holey carbon-coated TEM grids were used for sample mounting. Several images were collected at magnifications from 100,000 to 500,000 with a CCD camera. The software ImageJ® was used for particle size analysis in which diameter of at least 100 individual particles was measured. Further the number average ($D_{average}$) and the standard deviation (SD) were computed. Sauter's diameter (D_{Sauter}) (surface−volume diameter) was calculated using Eq. 1, where l_i is the number of particles having a diameter (d_i).

$$D_{Sauter} = \frac{\sum_{i=1}^{n} l_i d_i^3}{\sum_{i=1}^{n} l_i d_i^2} \tag{1}$$

Standard deviation for Sauter's diameter (SD_{Sauter}) was calculated as per Eq. 2, where SD is the standard deviation from TEM particle size analysis.

$$SD_{Sauter} = \left(\frac{\partial D_{Sauter}}{\partial d} \right) \cdot SD \tag{2}$$

Which is further expressed in Eq. 3

$$SD_{Sauter} = \left[3 - \frac{\left(2\sum_{i=1}^{n} d_i^3\right)\left(D_{average}\right)}{\left(\sum_{i=1}^{n} d_i^2\right)^2}\right] \cdot SD \qquad (3)$$

X-ray photoelectron spectroscopy (XPS) was performed on selected samples to determine the oxidation state of Zr in the synthesized catalysts. The analysis was carried out using a *Physical Electronics PHI 5000 Versa Probe* electron spectrometer system with monochromated aluminum (Al) Kα X-ray source at 1486.60 eV operated at 25 W, 15 kV, and 1 mA anode current. To reduce any possible charging effects of X-rays, a dual-beam charge neutralization method was applied, combining both low energy ions and electrons. The samples were previously outgassed in an ultrahigh vacuum chamber at 2.5×10^{-6} Pa for 12 h. Survey scans, as well as narrow scans (high-resolution spectra) were recorded with a 100 μm X-ray diameter spot size. The X-ray was used with a take-off angle of 45° for all samples. The survey spectra were collected from 0 to 1200 eV. The narrow Zr 3d spectra were collected from 174 to 194 eV. All of the spectra were obtained under identical conditions and calibrated against a value of the C 1s binding energy of 284.5 eV [29]. Measures on

selected samples were repeated at least three times on different spots; furthermore, on one sample the measurement was repeated from the beginning on a different portion of it, to estimate the precision of the values obtained. All measurements were affected by a standard deviation of about 0.4 eV. A commercial pure monoclinic nanometric (5–25 nm) ZrO_2 (*PlasmaChem GmbH*) was used as reference for the XPS data. Multipak 9.0 software was used to obtain semi-quantitative atomic percentage compositions. The peak position and areas were evaluated using symmetrical Gaussian–Lorentzian equations (in the fraction of 70 and 30%, respectively) with a Shirley-type background.

Results and discussion

Thermogravimetric analysis

ZrOPc/KB

The TGA profiles of ZrOPc/KB in Ar and H_2/Ar are shown in Fig. 2. No difference in ZrOPc decomposition was observed upon heat treatment under inert and reductive gas conditions. From both the weight loss curves a two-step decomposition process can be identified, with the first one between 180 and 350 °C, showing an inflection point (maximum weight loss rate) at 280 °C, and the second one between 450 and 650 °C and a maximum weight loss rate at 550 °C. It can be seen that after ∼750 °C nearly all ZrOPc has degraded, with weight loss being practically independent of the temperature.

TGA-MS of unsupported ZrOPc is shown in Fig. 3. In the first step at ∼300 °C benzonitrile (C_6H_5CN) (m/z = 103) fragments from the skeleton start breaking. The observed typical fractionation pattern of benzonitrile (m/z = 104, 76, 63, 50 not shown) [30] allows for a definite identification of m/z = 103 with benzonitrile. When the temperature reaches ∼500 °C, ZrOPc decomposition is still incomplete. This is confirmed by both TGA and MS signals which show rapid sample weight loss and C_6H_5CN signals, respectively. However, when the sample
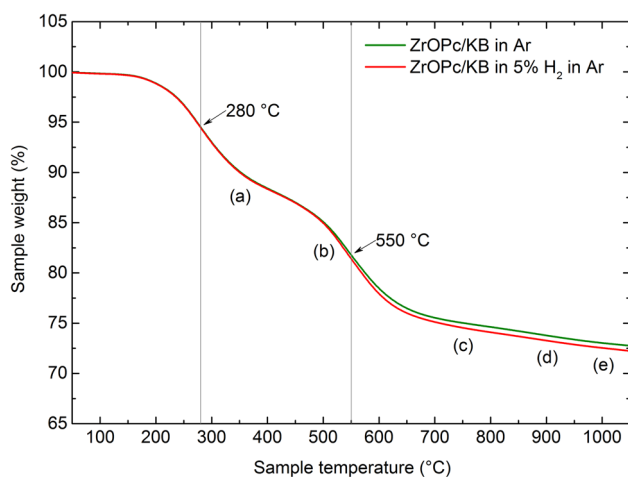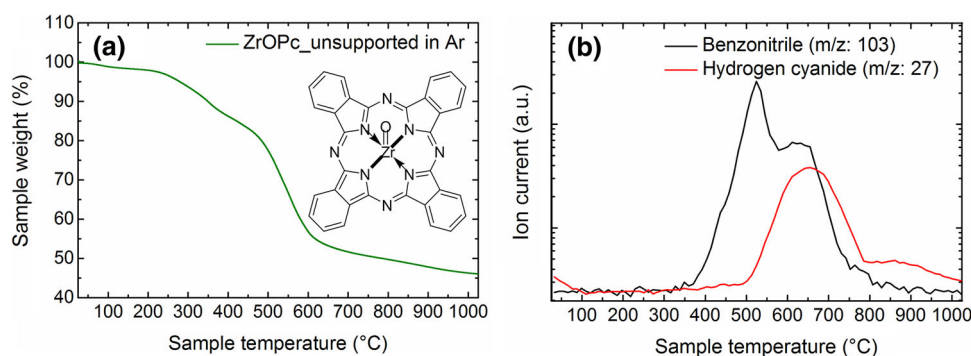

Fig. 2 Thermogravimetric analysis of ZrOPc/KB in pure Ar and 5% H_2/Ar atmospheres

Fig. 3 a Thermogravimetric and **b** mass spectrometry analysis of evolution products from unsupported ZrOPc in pure Ar atmosphere
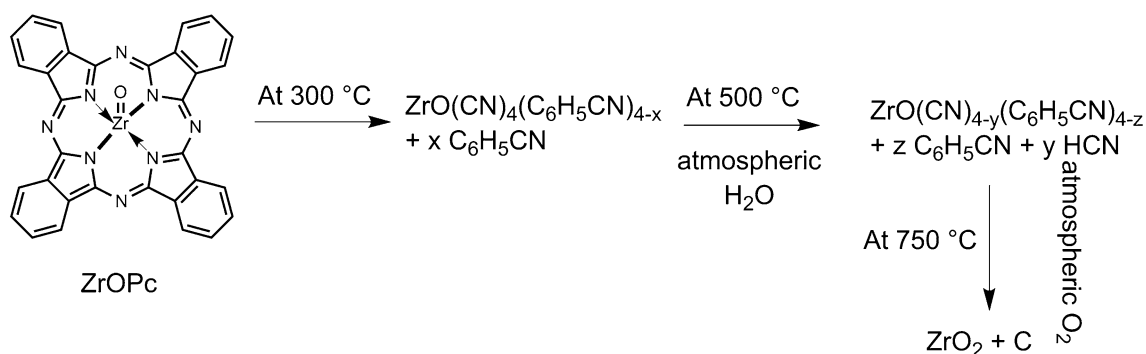
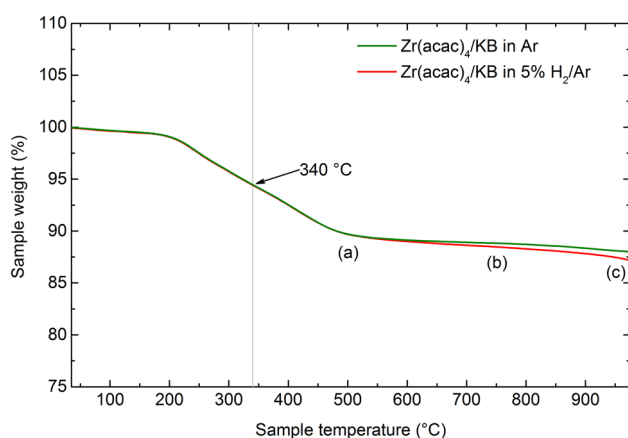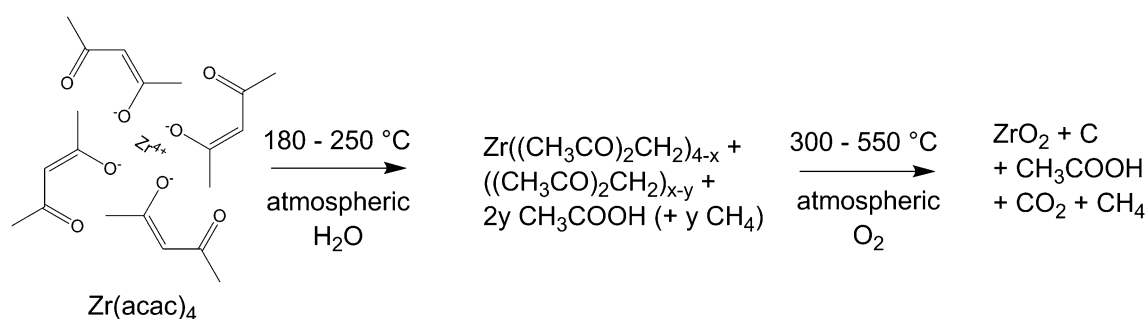**Fig. 4** Proposed mechanism for ZrOPc thermal degradation in pure Ar atmosphere

Fig. 5 Thermogravimetric analysis of Zr(acac)$_4$/KB in pure Ar and 5% H$_2$/Ar atmospheres

temperature reaches ~750 °C, nearly all the C$_6$H$_5$CN groups are detached from zirconium.

In addition to C$_6$H$_5$CN, hydrogen cyanide (HCN) (m/z = 27) and its fragments (m/z = 26, 12, 13 not shown) are detected between 500 and 800 °C [31], coming from the nitrile groups which chelate the zirconium atom. It can be concluded that molecular fragments in ZrOPc are stable until ~750 °C. ZrOPc thermal degradation proceeds through the proposed mechanism (Fig. 4). After 750 °C, ZrO$_2$ (confirmed by XRD, refer to the supplementary

information), and carbon from degraded molecular fragments of the intermediates remains. Ideally, no ZrO$_2$ should be formed as the TGA was done in pure Ar atmosphere, but atmospheric H$_2$O and O$_2$ through minor leaks in the instrument is the source of HCN and oxide formation.

From Fig. 2, it is clear that at 500 °C, decomposition of ZrOPc is not complete but after around 700 °C ZrOPc/KB has relatively stable weight. Five different temperatures were selected (a) 350 °C (b) 500 °C (c) 750 °C (d) 900 °C, and (e) 1000 °C to study the effect of heat-treatment temperatures on ZrOPc/KB (as marked in Fig. 2).

Zr(acac)$_4$/KB

Figure 5 shows the weight loss curve of Zr(acac)$_4$/KB upon heating in Ar and 5% H$_2$/Ar. One can easily see that the molecule degradation seems to follow the same path in both inert and reductive atmospheres. Only one-step degradation starting at ~200 °C was observed here; with the maximum weight loss rate at ~340 °C and a continuous weight loss until ~500 °C.

Thus, it shows less thermal stability compared to ZrOPc (Fig. 2). Unsupported Zr(acac)$_4$ was also analyzed with TGA-MS (Fig. 6). Between ~180 and ~250 °C we observe the highest and rapid weight loss (~45% of the initial weight, Fig. 6a, region I), thus most of the

Fig. 6 a Thermogravimetric and **b** mass spectrometry analysis of evolution products from unsupported Zr(acac)$_4$ in pure Ar atmosphere
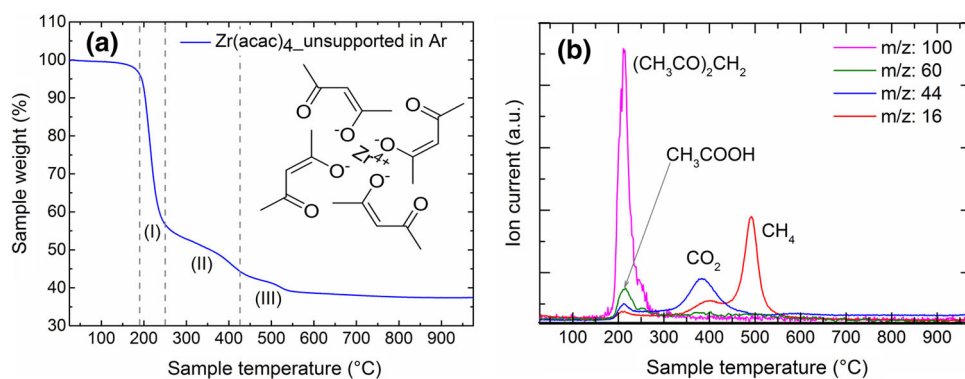
Fig. 7 Proposed mechanism for $Zr(acac)_4$ thermal degradation in pure Ar atmosphere

$Zr(acac)_4$ has degraded. From the MS-analysis we attribute this mainly to the detachment of acetylacetone $[(CH_3CO)_2CH_2]$ (m/z = 100, Fig. 6b and m/z = 85, 72, 58, 43 not shown) [32]. At the same temperature range acetic acid (CH_3COOH) is unambiguously identified by the characteristic mass signal at m/z = 60 (Fig. 6b), that in acetylacetone MS-pattern has a comparably low intensity [33].

Mass signals at m/z = 44 and 16 (Fig. 6b) are detected; they are attributed to acetylacetone and/or acetic acid (part of their standard MS-pattern). We cannot exclude the evolution of acetone (CH_3COCH_3) (m/z = 58) since it has

a MS-pattern that almost completely superimposes on the lower m/z mass-pattern of acetylacetone [34]. At a temperature slightly higher than $\sim 250\ °C$ the acetylacetone mass signal approaches zero (see Fig. 6b). Between 300 and 450 °C, carbon dioxide (CO_2) (m/z = 44) and acetic acid are observed as degradation products of $Zr(acac)_4$ [35] (Fig. 6a, region II). In the same temperature range, a mass signal at m/z = 16 (Fig. 6b) is detected; this is attributed to carbon dioxide and/or acetic acid as it is a part of their standard lower m/z MS-pattern. When the sample temperature reaches 450–550 °C there is a final weight loss of $\sim 4\%$ which is attributed to methane (CH_4) (m/z = 16), confirmed by its fragments (m/z = 15, 14, 13 not shown) [36] (Fig. 6a, region III). The observed molecular breakage pathway is in agreement with the reported literature [37]. $Zr(acac)_4$ degradation also yields ZrO_2 (confirmed by XRD, refer to the supplementary information) and carbon (Fig. 7).

As with ZrOPc, residual carbon in $Zr(acac)_4$ degradation is also attributed to the intermediate fragments.

At a temperature higher than 500 °C, $Zr(acac)_4$/KB attains a stable weight. Three different temperatures were selected (a) 500 °C (b) 750 °C, and (c) 950 °C to study the effect of heat-treatment conditions on the final product (Fig. 5).

Heat treatment of carbon-supported precursors

ZrOPc/KB

Due to the high thermal stability of ZrOPc (discussion from Figs. 2, 3, 4, 5, 6), we maintained 2 h of RED conditions before PO conditions. This was to ensure complete removal of the organic fragments from ZrOPc.

XRD patterns of the heat treated samples are shown in Fig. 8. For the sample heat treated at 350 °C under PO conditions no ZrO_2 formation was observed (diffractogram not shown), which was further confirmed by TEM measurements, where no particles were found. For samples heat-treated in PO gas conditions, the formation of ZrO_2 phase was observed for treatment at 500 °C and above.
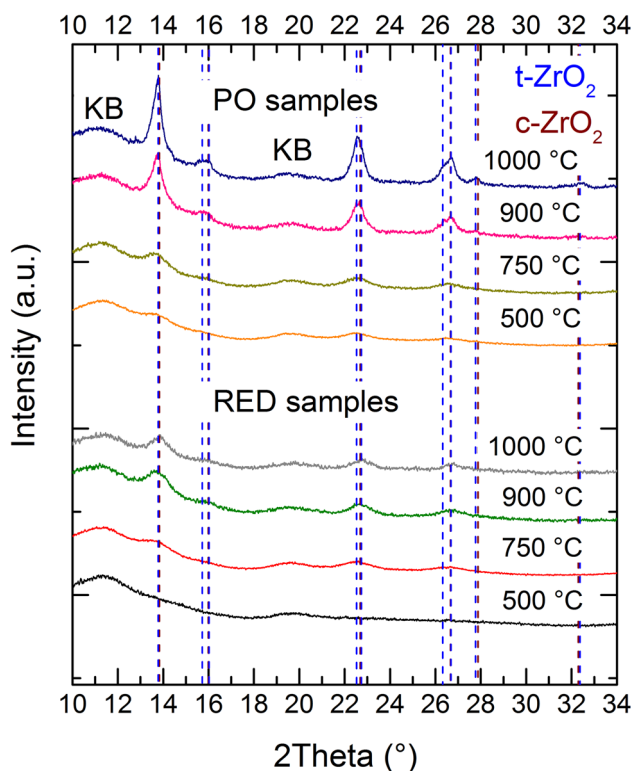

Fig. 8 X-ray diffractograms of ZrOPc/KB heat-treated at different temperatures in PO and RED gas conditions. KB is Ketjenblack carbon support with reflexes at positions similar to graphite (PDF no. 00-056-0159)

With the increase in treatment temperature, full width half maximum (FWHM) of the reflections decreases, clearly indicating an increase in nanoparticle crystallinity.

For the samples heat-treated in RED conditions (Fig. 8), no diffraction pattern related to ZrO_2 was detected for samples treated at 350 (diffractogram not shown) and 500 °C. This result fits well with the TGA data of ZrOPc/KB which clearly show that at 350 and 500 °C the phthalocyanine macrocycle degradation was incomplete with some organic residues remaining which might hinder oxidation of the metal center (see mass spectrometer data in Fig. 3). For higher synthesis temperatures (≥750 °C), broad ZrO_2 reflections were observed, which clearly indicated the formation of ZrO_2. In particular, for heat-treatment temperatures ≥900 °C, ZrO_2 reflections from RED samples show higher FWHM compared to that of PO samples prepared at the same temperature. The results suggest that, at synthesis temperatures ≥900 °C PO gas conditions facilitates the formation of larger crystallites.

For the heat-treated samples correct phase assignment for the synthesized ZrO_2 was not trivial.

This was because the reflections were broad and the standard tetragonal (t) and cubic (c) phase reflections were nearly overlapping. The main difference is only a shoulder reflection at 26.32° for t-ZrO_2 (marked by a red asterisk, Fig. 9). The reflections of the high temperature
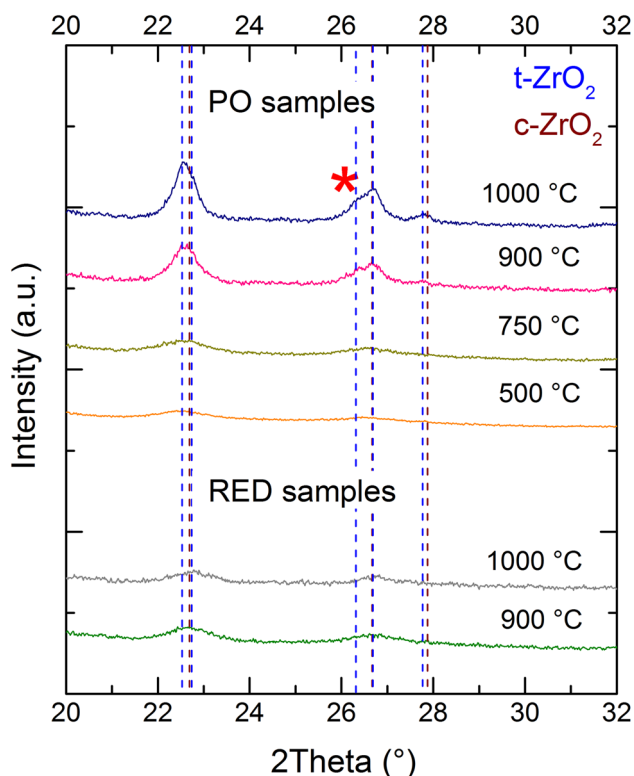
Fig. 9 ZrO_2 phase identification in heat-treated ZrOPc/KB samples

PO samples (900 and 1000 °C) fit very well with the reference data of a t-ZrO_2 phase (PDF no. 01-072-7115). The particle size is estimated to be dominantly below 20 nm based on the broadening of the reflections. No specific ZrO_2 phase was assignable for the samples synthesized at lower temperatures (500 and 750 °C) in PO conditions due to broad reflections. Also for all the samples synthesized in RED conditions no definite ZrO_2 phase is assignable. Thus, at synthesis temperatures ≥900 °C, PO gas conditions are important in formation of nanocrystals in which t-ZrO_2 phase can be clearly identified.

Figure 10 shows TEM micrographs of the supported ZrO_2 nanoparticles prepared from ZrOPc/KB. For the samples prepared under PO gas conditions (Fig. 10a–d, f), a gradual increase in particle size with heat treatment temperature was observed. This is further confirmed in Table 1, showing that the average size of synthesized ZrO_2 nanoparticles enlarged from 4 to 9 nm with an increase in synthesis temperature from 500 to 1000 °C. Comparing the heat-treated ZrOPc/KB sample under RED conditions at 1000 °C with samples heat-treated in PO conditions, it is observed that PO conditions clearly facilitate particle growth (Fig. 10d–f). Since Zr in phthalocyanine is chelated by N_4 of the complex, a possible reason for the faster ZrO_2 growth in PO heat treatment is the assistance of dilute oxygen in degrading the N_4 chelate. Evaluation of TEM micrographs of PO samples confirms the particle size trend from XRD analysis (Figs. 8, 10).
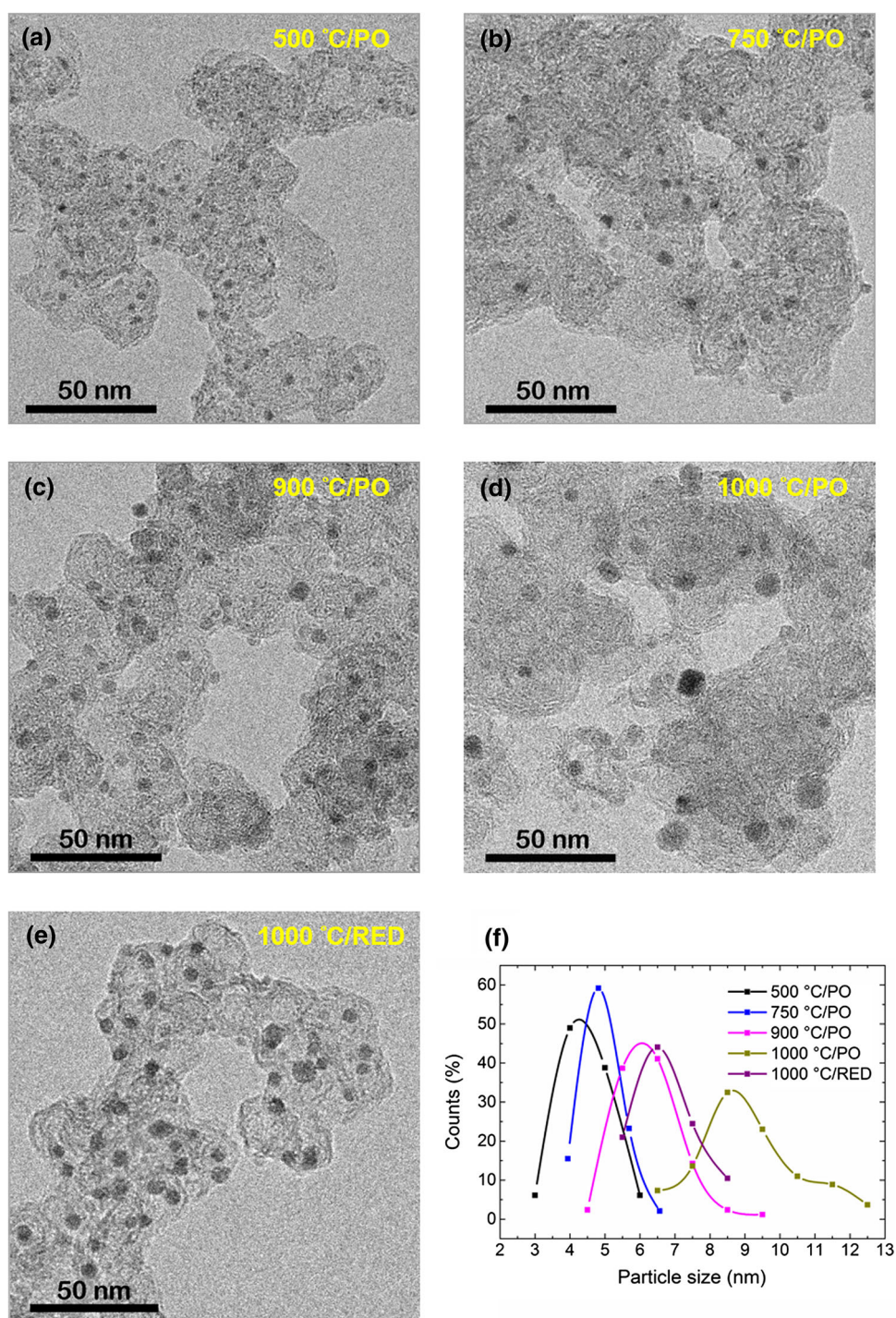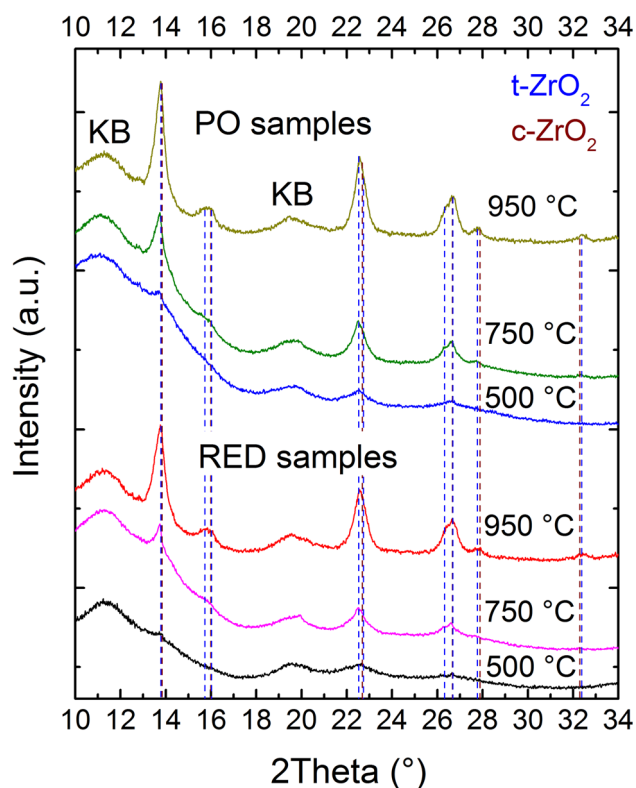
Zr(acac)₄/KB

From the diffractograms, ZrO_2 formation is confirmed for samples synthesized in both PO and RED conditions (Fig. 11). These results fit well with the data obtained from TGA for Zr(acac)₄/KB, which clearly show that acetylacetonate degradation is nearly complete at 500 °C (Fig. 5). This means that at this temperature the metal atom can easily get oxidized. Thus, lower thermal stability and/or higher molecular oxygen from Zr(acac)₄ makes ZrO_2 formation easier.

Further, as the heat treatment temperature is increased, an increase in the ZrO_2 crystallite size is observed. In addition, FWHM of ZrO_2 reflections from samples heat-treated at 950 °C under PO and RED conditions seem very similar.

For the samples heat-treated at 750 and 950 °C in PO and RED conditions, a t-phase is assigned to the synthesized ZrO_2 due to the presence of the shoulder reflection at 26.32° (PDF no. 01-072-7115) (marked by a violet asterisk, Fig. 12). No specific ZrO_2 phase is assignable to samples synthesized at 500 °C in PO and RED conditions due to very broad reflections. Thus, from the observations on XRD patterns, we can conclude that ZrO_2 synthesized from ZrOPc at ≥900 °C under

Fig. 10 TEM images of supported ZrO_2 nanoparticles from ZrOPc/KB heat-treated at different temperatures under PO conditions (**a**–**d**): **a** 500 °C; **b** 750 °C; **c** 900 °C; **d** 1000 °C; **e** under RED conditions 1000 °C and **f** particle size distribution plot of the samples shown here

PO conditions and from $Zr(acac)_4$ at ≥ 750 °C under both PO and RED conditions is isostructural.

In Fig. 13a, b, d, an increase in the average particle size from 6.5 to ~ 10 nm can be observed in the samples as the heat-treatment temperature is increased from 750 to 950 °C. Comparing b and c, no major difference in the particle size is seen. The similarity in particle size is further confirmed in Fig. 13d and Table 1. This clearly indicates

that heat-treatment gas conditions are not influencing particle growth, which is in contrast with ZrOPc/KB samples Fig. 10f. This difference is attributed to lower $Zr(acac)_4$ thermal stability and its higher oxygen content. Observations from TEM analysis are in congruence with the trends observed in diffractograms of $Zr(acac)_4$ samples (Fig. 11). Dispersion of ZrO_2 nanoparticles from $Zr(acac)_4$ and ZrOPc precursor is similar (Figs. 10, 13).

Fig. 11 X-ray diffractograms of Zr(acac)₄/KB heat-treated at different temperatures in PO and RED gas conditions. KB is Ketjenblack carbon support with reflexes at positions similar to graphite (PDF no. 00-056-0159)

Fig. 12 ZrO_2 phase identification in heat-treated Zr(acac)₄/KB samples

ZrO_2 crystallite size calculations, particle size analysis from TEM and its Sauter's diameter (surface-volume diameter) have been summarized in Table 1.

From Table 1, it is evident that crystallite size calculations from XRD and particle size analysis from TEM are significantly in agreement. This infers that ZrO_2 nanoparticles are nanocrystals, and the amorphous phase should be negligible in the samples which are synthesized at temperatures ≥750 °C. There is also a good agreement between average particle size and Sauter's diameter calculations, which further confirms that all the samples have a narrow size distribution.

Variation of ZrO_2 loading

t-ZrO_2 phase formation is apparent (PDF no. 01-072-7115) in 15 and 10 wt.% ZrO_2/KB samples, while it is not attributable in 5 wt.% sample due to very broad reflections (Fig. 14). As the loading increases, FWHM of ZrO_2 reflections decreases. This infers an increase in the oxide particle size.

This increase in ZrO_2 particle size is confirmed in the TEM analysis (see Fig. 15), with a particle size ranging

from ∼5 to 8.5 nm in the samples as the loading increases from 5 to 15 wt.%. These observations are complementary with the FWHM trends from XRD (Fig. 14). Based on TEM micrographs the nanoparticles are well-dispersed on the support without obvious agglomeration and the dispersion looks similar for all the three samples. An attempt to calculate the average inter-particle distance (AID) for the above samples has been performed. In the literature about carbon supported platinum catalysts, several approaches have been followed to estimate the inter-particle distance on the support surface. Meier et al. proposed one of these methods, which as a rule-of-thumb is an estimate for AID (adapted here for carbon supported zirconia nanoparticles) (Eq. 4) [38]:

$$AID = \sqrt{\frac{\pi}{3\sqrt{3}} \cdot 10^{-3} \cdot \rho_{ZrO_2} \cdot \frac{100 - L_{ZrO_2}}{L_{ZrO_2}} \cdot A_{carbon} \cdot D_{average}^3} - D_{average}$$

(4)

where $\rho_{ZrO_2} = 6.1 \, \text{g/cm}^3$ is the density of tetragonal zirconia, L_{ZrO_2} is the loading of ZrO_2 on the catalyst powder in percent, $A_{carbon} = 800 \, \text{m}^2/\text{g}$ for Ketjenblack E-type [39], and $D_{average}$ has the same meaning as defined before.

Fig. 13 TEM images of supported ZrO_2 nanoparticles from $Zr(acac)_4$/KB heat-treated at different temperatures under PO conditions (**a, b**): **a** 750 °C; **b** 950 °C; **c** under RED conditions 950 °C; **d** and particle size distribution plot of the samples shown here
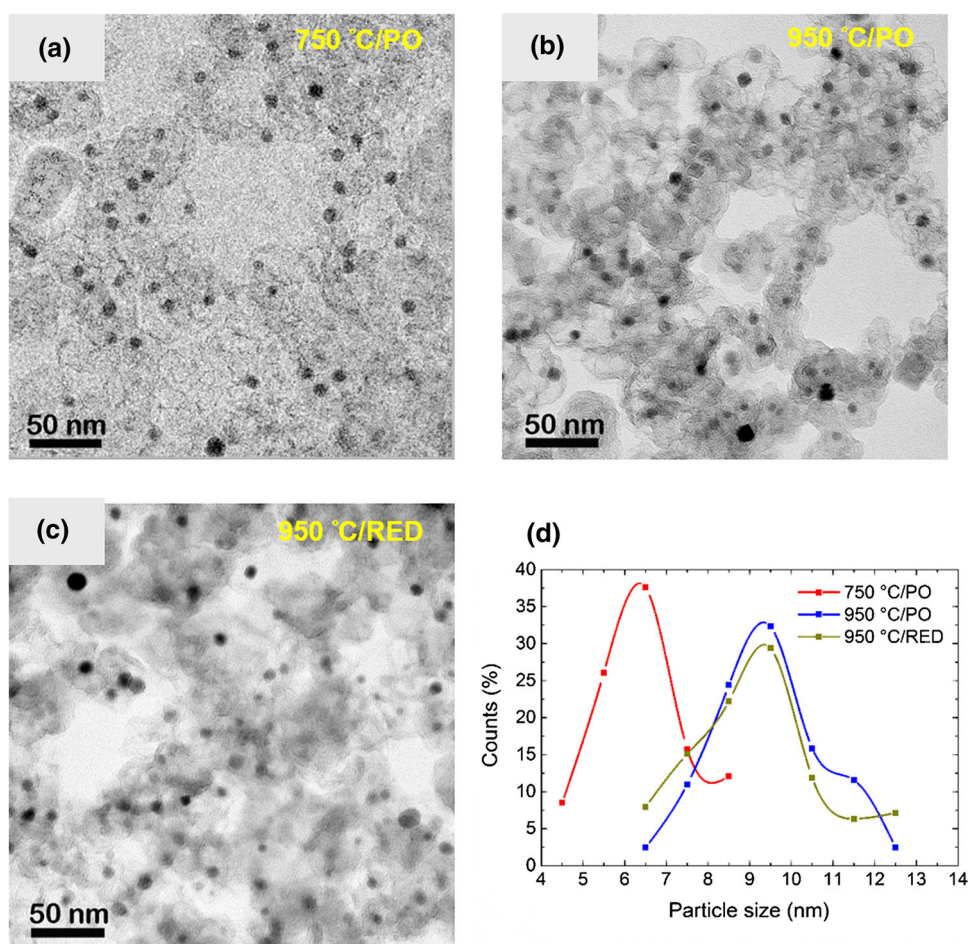

Table 1 Crystallite size based on Scherrer equation ($k = 0.94$) ($D_{Scherrer}$), average particle size ($D_{average}$) analysis with standard deviation (SD), and Sauter's diameter (D_{Sauter}) with standard deviation for Sauter's diameter (SD_{Sauter}) from particle size analysis of TEM images of ZrOPc/KB and $Zr(acac)_4$/KB samples heat-treated at different temperatures and gas conditions

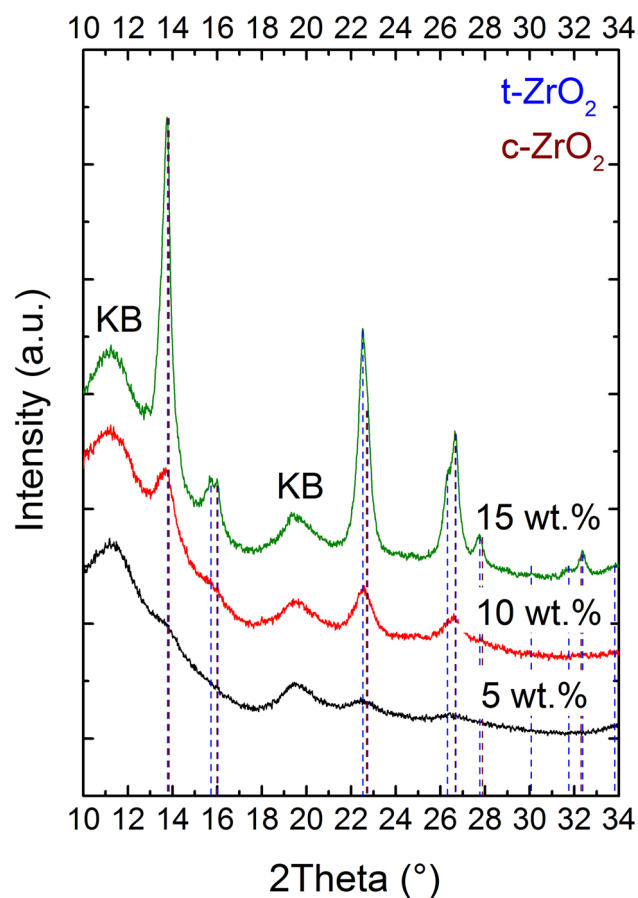| Sample (°C)		$D_{Scherrer}$ (nm)	$D_{average} \pm$ SD (nm)	$D_{Sauter} \pm SD_{Sauter}$ (nm)
Heat-treated ZrOPc/KB				
PO	500	4	4 ± 1	5 ± 1
	750	4.5	5 ± 1	5 ± 1
	900	8	6.5 ± 1	7 ± 1
	1000	9	9 ± 2	10 ± 2
RED	500	–	–	–
	750	4	4 ± 1	4 ± 1
	900	4.5	5.5 ± 1	6 ± 1
	1000	5	7 ± 2	7 ± 2
Heat-treated $Zr(acac)_4$/KB				
PO	500	5	3.5 ± 1	3.5 ± 1
	750	7	6.5 ± 2	7 ± 2
	950	8.5	10 ± 2	10 ± 2
RED	500	–	3.5 ± 1	3.5 ± 1
	750	5.5	5 ± 1	5 ± 1
	950	8	9 ± 2	10 ± 2

Fig. 14 X-ray diffractograms of ZrOPc/KB heat-treated at 950 °C in PO gas conditions with varied ZrO_2 loadings. KB is Ketjenblack carbon support with reflexes at positions similar to graphite (PDF no. 00-056-0159)

If one calculates the AID for the samples shown if Fig. 15, the values range from ≈80–95 nm (Table 2). Thus, although the loadings differ by a maximum factor of three, the apparent particle density on the support surface remains only weakly influenced.

From Table 2 we can also conclude in this case that the synthesized nanoparticles are nanocrystals which grow in size as ZrO_2 loading increases. Thus, metal loading could be used to tune the size of the supported nanocrystals.

X-ray photoelectron spectroscopy

X-ray photoelectron spectroscopy (XPS) is a sensitive tool for analyzing the chemical state of Zr cations in ZrO_2. Figure 16 shows the high-resolution Zr 3d spectra of samples prepared in various conditions. All of the spectra show the typical doublet structure in $3d_{5/2}$ and $3d_{3/2}$

components, due to the spin–orbit splitting of the 3d level. The peaks resulted ranging from 182.3 to 183.4 eV for Zr $3d_{5/2}$, and from 184.7 to 185.7 eV for Zr $3d_{3/2}$, as shown in shaded bands in Fig. 16. In particular, sample ZrOPc/KB 900 °C/PO (which is one of the most interesting catalyst on the electrochemical point of view [26]) shows the measured spectra with Gaussian–Lorentzian fits and a Shirley type background. The deconvolution of the Zr 3d spin–orbit doublet is in agreement with the existence of Zr^{4+} [40, 41]. Similar analyses has been performed for other samples. Zr $3d_{5/2}$ values are extracted by taking the peak positions after data-fitting and reported in Fig. 17, together with the standard deviation (±0.4 eV).

After comparing the binding energy of Zr^{4+} of pure monoclinic ZrO_2 (internal reference: 181.9 eV) with those reported in literature 181.9–182.1 eV [41–44] (green shaded band in Fig. 17), we could confirm that all the measurements were in agreement with reference values. The measured binding energies of Zr $3d_{5/2}$ in all the samples lie inside or close to the range of Zr^{4+} species in pure tetragonal ZrO_2 182.1–182.8 eV [40, 41, 44–47] (yellow shaded band in Fig. 17).

Thus, the formation of ZrO_2 is confirmed by XPS for all the examined synthesis routes. Considering the trends of the binding energy of the Zr $3d_{5/2}$ peak with the synthesis conditions (Fig. 17) and the standard deviation linked with the XPS measurements, it is not possible to obtain a clear trend between Zr $3d_{5/2}$ with temperature, heat treatment gas conditions, and oxide particle size. In addition, it is impossible to link the shift of the binding energy with the presence of oxygen vacancies. The presence of suboxides must be excluded since in XRD we do not detect them and similar average ZrO_2 particle size from XRD and TEM demonstrate the only presence of pure ZrO_2 (Figs. 8, 11; Table 1).

Conclusions

Successful synthesis of pure carbon supported ZrO_2 nanoparticles has been reported in this paper. A thorough comparative study on the synthesis of metal-oxide nanoparticles from two different precursors namely, ZrOPc and $Zr(acac)_4$ has been done. Our aim is to optimize the nanoparticle size and crystallinity of the samples for the possible application as electrocatalysts for the oxygen reduction reaction in PEMFCs. Using thermogravimetric analysis coupled with mass spectrometry, we could show and confirm the thermal-decomposition behavior of the

Fig. 15 TEM images of carbon supported ZrO_2 nanoparticles from ZrOPc/KB with different loadings: **a** 5 wt.%; **b** 10 wt.%; **c** 15 wt.% and **d** particle size distribution plot of the samples shown here
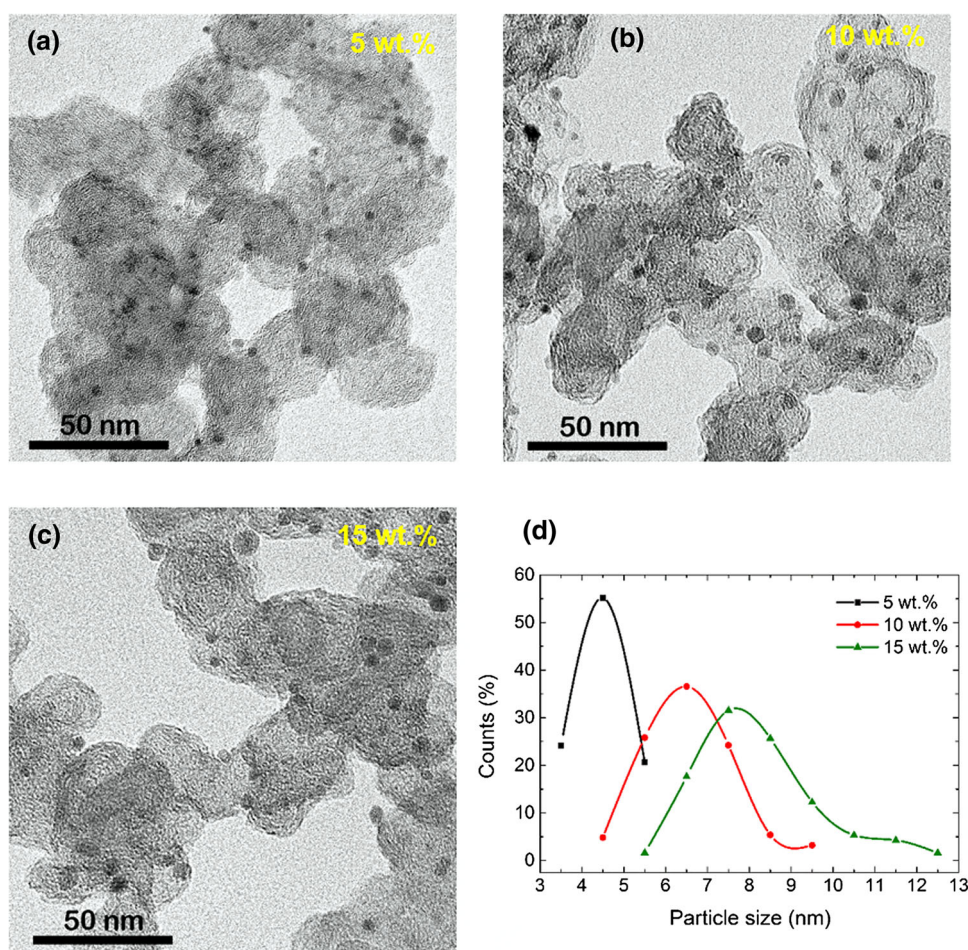

Table 2 Crystallite size based on Scherrer equation ($k = 0.94$) ($D_{Scherrer}$), average particle size ($D_{average}$) analysis with standard deviation (SD), and Sauter's diameter (D_{Sauter}) with standard deviation for Sauter's diameter (SD_{Sauter}) from particle size analysis of TEM images of ZrOPc/KB samples with varied loadings, but heat-treated at same conditions. Average inter-particle distance (AID) with standard deviation (SD_{AID}) from Eq. 4

Sample (wt.%)	$D_{Scherrer}$ (nm)	$D_{average} \pm$ SD (nm)	$D_{Sauter} \pm SD_{Sauter}$ (nm)	AID $\pm SD_{AID}$ (nm)
5	4.5	5 ± 1	5 ± 1	79 ± 25
10	5.5	7 ± 1	7 ± 1	88 ± 20
15	8.5	8.5 ± 2	9 ± 2	93 ± 36

chosen precursors. A clear correlation between the results from thermal analysis of precursors and the size- and structure of the nanoparticles obtained after heat-treatment at different temperatures was clearly seen. We showed that ZrO_2 formation happens at a lower temperature with $Zr(acac)_4$ than with ZrOPc, due to the lower thermal stability of acetylacetonate precursor and a higher content of oxygen in comparison to phthalocyanine. With ZrOPc at heat-treatment temperatures ≥ 900 °C, PO conditions facilitate crystallite growth and formation of distinct t-ZrO_2, but with $Zr(acac)_4$ a distinct t-ZrO_2 phase

formation is observed already at temperatures ≥ 750 °C in both PO and RED conditions, due to the presence of a stoichiometrical excess of oxygen already in the precursor. The oxide nanoparticles in all the samples are well-distributed on the carbon support without evident agglomeration. After the size- and structural- analysis of the oxide nanoparticles, it is concluded that the oxide nanoparticles are nanocrystals and the amorphous phase is negligible in samples heat-treated at temperatures ≥ 750 °C. From the loading variation of zirconium, we show that metal loading can also be used to tune the size of oxide nanocrystals.

Fig. 16 High resolution XPS spectra of Zr 3d core level of carbon supported ZrOPc and Zr(acac)$_4$ heat-treated at different temperatures in PO and RED gas conditions. The shaded bands highlight the binding energies variability of the samples
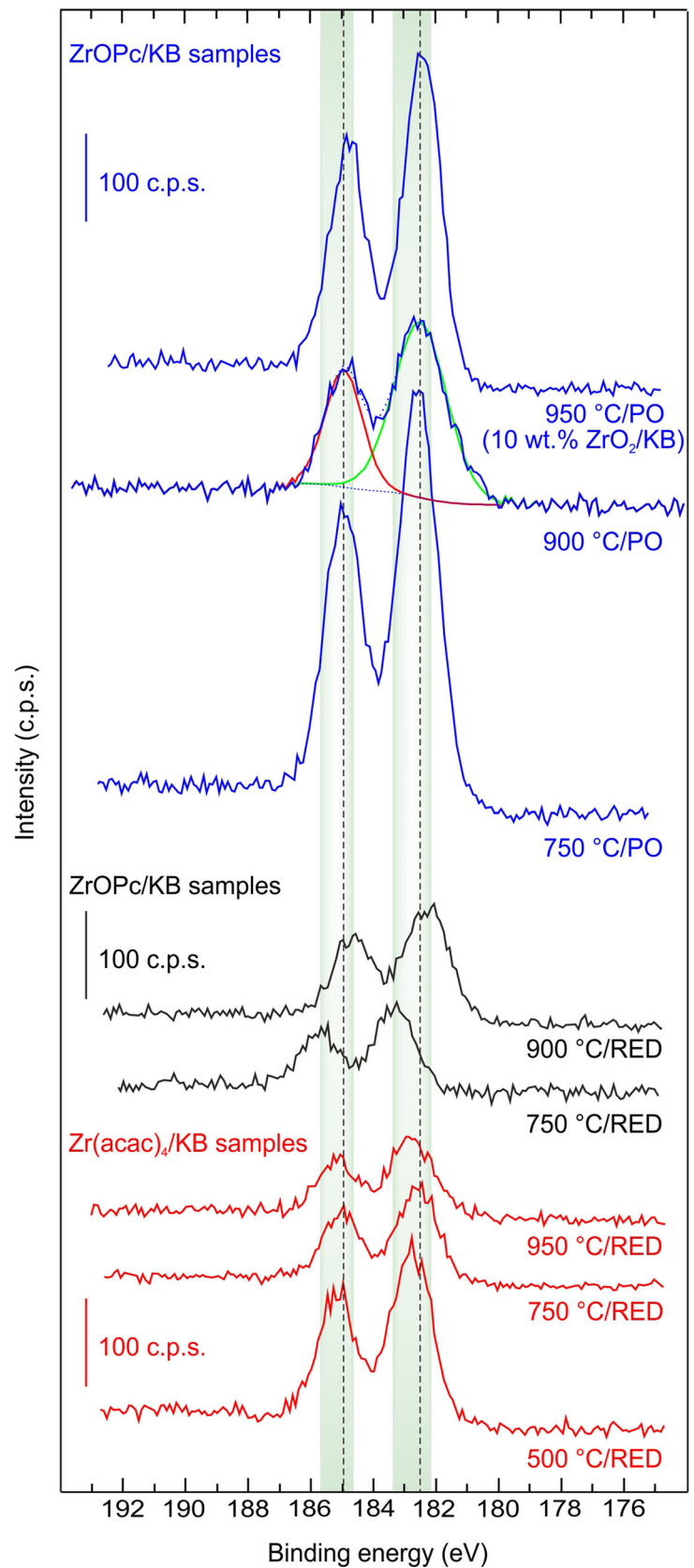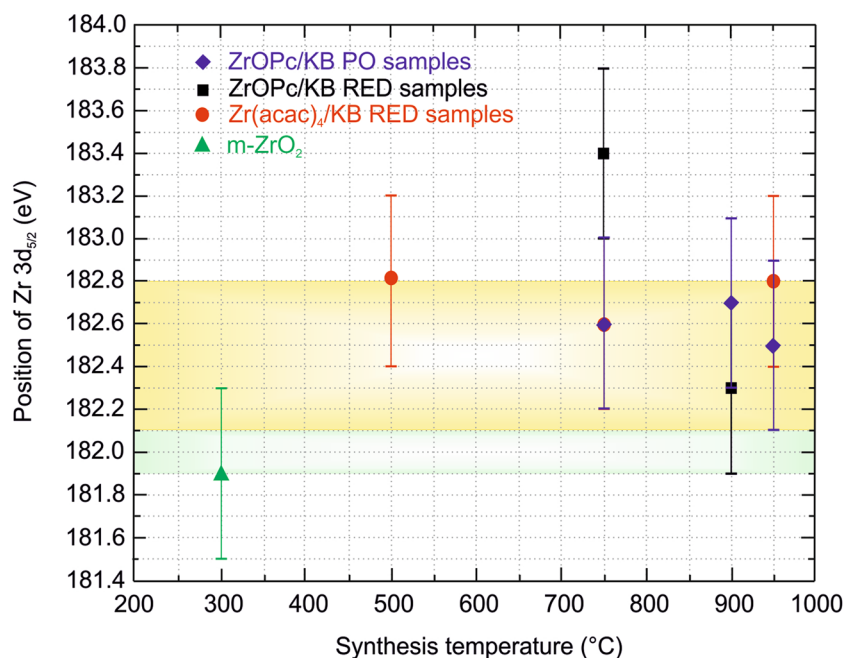
Fig. 17 Binding-energy shift of the Zr 3d$_{5/2}$ peak of heat-treated samples as a function of the synthesis temperature and gas conditions, together with the measured value of the commercial m-ZrO$_2$. The ranges of binding energies from the literature for m-ZrO$_2$ [41–44] and t-ZrO$_2$ [40, 41, 44–47] are depicted by the shaded green and yellow bands, respectively

From XPS analysis, it is clear that Zr species in samples from different synthesis routes are in the pure ZrO$_2$ state. No clear trend between Zr 3d$_{5/2}$ binding energy and synthesis temperature or gas conditions was found.

References

1. Earnshaw, A., Greenwood, N.: Chemistry of the elements, 2nd edn. Butterworth-Heinemann, Oxford (1998)
2. Shukla, S., Seal, S.: Mechanisms of room temperature metastable tetragonal phase stabilisation in zirconia. Int. Mater. Rev. **50**, 45–64 (2005)
3. French, R., Glass, S., Ohuchi, F., Xu, Y., Ching, W.: Experimental and theoretical determination of the electronic structure and optical properties of three phases of ZrO2. Phys. Rev. B **49**, 5133–5142 (1994)
4. Minh, N.: Ceramic fuel cells. J. Am. Ceram. Soc. **76**, 563–588 (1993)
5. Schulz, U., Leyens, C., Fritscher, K., Peters, M., Saruhan-Brings, B., Lavigne, O., Dorvaux, J.-M., Poulain, M., Mévrel, R., Caliez, M.: Some recent trends in research and technology of advanced thermal barrier coatings. Aerosp. Sci. Technol. **7**, 73–80 (2003)
6. Kosmač T, Oblak Č, Jevnikar P, Funduk N, Marion L.: Strength and reliability of surface treated Y-TZP dental ceramics. J. Biomed. Mater. Res. **53**, 304–313 (2000)
7. Guo, D., Qiu, X., Zhu, W., Chen, L.: Synthesis of sulfated ZrO2/MWCNT composites as new supports of Pt catalysts for direct methanol fuel cell application. Appl. Catal. B **89**, 597–601 (2009)
8. Lv, H., Cheng, N., Peng, T., Pan, M., Mu, S.: High stability platinum electrocatalysts with zirconia–carbon hybrid supports. J. Mater. Chem. **22**, 1135–1141 (2012)
9. Qu, W., Wang, Z., Sui, X., Gu, D., Yin, G.: ZrC-C and ZrO2-C as novel supports of Pd catalysts for formic acid electrooxidation. Fuel Cells **13**, 149–157 (2013)
10. Malolepszy, A., Mazurkiewicz, M., Stobinski, L., Lesiak, B., Kövér, L., Tóth, J., Mierzwa, B., Borodzinski, A., Nitze, F., Wågberg, T.: Deactivation resistant Pd–ZrO2 supported on multiwall carbon nanotubes catalyst for direct formic acid fuel cells. Int. J. Hydrog. Energy **40**, 16724–16733 (2015)
11. Rutkowska, I., Kulesza, P.: Electrocatalytic oxidation of ethanol in acid medium: enhancement of activity of vulcan-supported platinum-based nanoparticles upon immobilization within nanostructured zirconia matrices. Funct. Mater. Lett. **7**, 1440005 (2014)
12. Cheng-Lan, L., Yu-Chi, Y.: Platinum nanoparticles supported on zirconia–carbon black nanocomposites for methanol oxidation reaction. Res. Chem. Intermed. **40**, 2207–2215 (2014)
13. Wang, R., Wang, K., Wang, H., Wang, Q., Key, J., Linkov, V., Ji, S.: Nitrogen-doped carbon coated ZrO2 as a support for Pt nanoparticles in the oxygen reduction reaction. Int. J. Hydrog. Energy **38**, 5783–5788 (2013)
14. Seo, J., Cha, D., Takanabe, K., Kubota, J., Domen, K.: Electrodeposited ultrafine NbOx ZrOx and TaOx nanoparticles on carbon black supports for oxygen reduction electrocatalysts in acidic media. ACS Catal. **3**, 2181–2189 (2013)

15. Sebastián, D., Baglio, V., Sun, S., Tavares, A., Aricò, A.: Facile synthesis of Zr- and Ta-based catalysts for the oxygen reduction reaction. Chin. J. Catal. **36**, 484–489 (2015)

16. Liu, Y., Ishihara, A., Mitsushima, S., Kamiya, N., Ota, K.: Zirconium oxide for PEFC cathodes. Electrochem. Solid-State Lett. **8**, A400–A402 (2005)

17. Ohgi, Y., Ishihara, A., Matsuzawa, K., Mitsushima, S., Ota, K.: Zirconium oxide-based compound as new cathode without platinum group metals for PEFC. J. Electrochem. Soc. **157**, B885–B891 (2010)

18. Shao, M.: Electrocatalysis in fuel cells: A non- and low- platinum approach. Springer, London (2013)

19. Yin, S., Ishihara, A., Kohno, Y., Matsuzawa, K., Mitsushima, S., Ota, K.: Preparation of highly active Zr Oxide-based oxygen reduction electrocatalysts as PEFC cathode. ECS Trans. **50**, 1785–1790 (2013)

20. Yin, S., Ishihara, A., Kohno, Y., Matsuzawa, K., Mitsushima, S., Ota, K.: Enhancement of oxygen reduction activity of zirconium oxide-based cathode for PEFC. ECS Trans. **58**, 1489–1494 (2013)

21. Okada, Y., Ishihara, A., Arao, M., Matsumoto, M., Imai, H., Kohno, Y., Matsuzawa, K., Mitsushima, S., Ota, K.: Improvement of the electrocatalytic activity of zirconium oxide-based catalyst for ORR. ECS Trans. **64**, 231–238 (2014)

22. Mecheri, B., Iannaci, A., D'Epifanio, A., Mauri, A., Licoccia, S.: Carbon-supported zirconium oxide as a cathode for microbial fuel cell applications. ChemPlusChem **81**, 80–85 (2016)

23. Lee, S., Zhang, Z., Wang, X., Pfefferle, L., Haller, G.: Characterization of multi-walled carbon nanotubes catalyst supports by point of zero charge. Catal. Today **164**, 68–73 (2011)

24. Leznoff, C., Lever, A.: Phthalocyanines: properties and applications. Wiley, New York (1989)

25. Stary, J., Liljenzin, J.: Critical evaluation of equilibrium constants involving acetylacetone and its metal chelates. Pure Appl. Chem. **54**, 2557–2592 (1982)

26. Mittermeier, T., Madkikar, P., Wang, X., Gasteiger, H., Piana, M.: ZrO2 based oxygen reduction catalysts for PEMFCs: towards a better understanding. J. Electrochem. Soc. **163**, F1543–F1552 (2016)

27. Tomachynski, L., Chernii, V., Volkov, S.: Synthesis of dichloro phthalocyaninato complexes of titanium, zirconium, and hafnium. Russ. J. Inorg. Chem. **47**, 208–211 (2002)

28. Catanorchi S., Piana M.: High performance ORR (oxygen reduction reaction) pgm (pt group metal) free catalyst. Google Patents. http://www.google.com.ar/patents/US20110034325 (2011). Accessed 17 April 2015

29. Liu, G., Li, X., Ganesan, P., Popov, B.: Studies of oxygen reduction reaction active sites and stability of nitrogen-modified carbon composite catalysts for PEM fuel cells. Electrochim. Acta **55**, 2853–2858 (2010)

30. National Institute of Standards and Technology. Benzonitrile. http://webbook.nist.gov/cgi/cbook.cgi?ID=C100470&Units=SI&Mask=200#Mass-Spec. Accessed 03 Mar 2015

31. Cornu, A., Massot, R.: Compilation of mass spectral data/Index de Spectres de Masse. Heyden & Sons, London (1966)

32. National Institute of Standards and Technology. Acetylacetone. http://webbook.nist.gov/cgi/cbook.cgi?ID=C123546&Mask=200#Mass-Spec. Accessed 17 April 2015

33. National Institute of Standards and Technology. Acetic acid. http://webbook.nist.gov/cgi/cbook.cgi?ID=C64197&Mask=200#Mass-Spec. Accessed 17 April 2015

34. National Institute of Standards and Technology. Acetone. http://webbook.nist.gov/cgi/cbook.cgi?ID=67-64-1&Units=SI&cMS=on. Accessed 17 April 2015

35. National Institute of Standards and Technology. Carbon dioxide. http://webbook.nist.gov/cgi/cbook.cgi?ID=C124389&Units=SI&Mask=200#Mass-Spec. Accessed 17 April 2015

36. National Institute of Standards and Technology. Methane. http://webbook.nist.gov/cgi/cbook.cgi?Formula=CH4&NoIon=on&Units=SI&cMS=on. Accessed 17 April 2015

37. Jasim, F.: Simultaneous thermal analysis of zirconium(IV) acetylacetonate in a helium atmosphere. J. Therm. Anal. **37**, 149–153 (1991)

38. Meier, J., Galeano, C., Katsounaros, I., Witte, J., Bongard, H., Topalov, A., Baldizzone, C., Mezzavilla, S., Schüth, F., Mayrhofer, K.: Design criteria for stable Pt/C fuel cell catalysts. Beilstein J. Nanotechnol. **5**, 44–67 (2014)

39. Meini, S., Piana, M., Beyer, H., Schwämmlein, J., Gasteiger, H.: Effect of carbon surface area on first discharge capacity of Li-O2 cathodes and cycle-life behavior in ether-based electrolytes. J. Electrochem. Soc. **159**, A2135–A2142 (2012)

40. Ram, S., Mondal, A.: X-ray photoelectron spectroscopic studies of Al3 + stabilized t-ZrO2 of nanoparticles. Appl. Surf. Sci. **221**, 237–247 (2004)

41. Basahel, S., Ali, T., Mokhtar, M., Narasimharao, K.: Influence of crystal structure of nanosized ZrO2 on photocatalytic degradation of methyl orange. Nanoscale Res. Lett. **10**, 1–13 (2015)

42. Majumdar, D., Chatterjee, D.: X-ray photoelectron spectroscopic studies on yttria, zirconia, and yttria-stabilized zirconia. J. Appl. Phys. **70**, 988–992 (1991)

43. Guittet, M., Crocombette, J., Gautier-Soyer, M.: Bonding and XPS chemical shifts in ZrSiO4 versus SiO2 and ZrO2: charge transfer and electrostatic effects. Phys. Rev. B **63**, 125117 (2001)

44. Kuratani, K., Uemura, M., Mizuhata, M., Kajinami, A., Deki, S.: Novel fabrication of high-quality ZrO2 ceramic thin films from aqueous solution. J. Am. Ceram. Soc. **88**, 2923–2927 (2005)

45. Ardizzone, S., Bianchi, C.: XPS characterization of sulphated zirconia catalysts: the role of iron. Surf. Interface Anal. **30**, 77–80 (2000)

46. Alvarez, M., López, T., Odriozola, J., Centeno, M., Domínguez, M., Montes, M., Quintana, P., Aguilar, D., González, R.: 2,4-Dichlorophenoxyacetic acid (2,4-D) photodegradation using an Mn +/ZrO2 photocatalyst: XPS, UV–vis, XRD characterization. Appl. Catal. B **73**, 34–41 (2007)

47. Brenier, R., Mugnier, J., Mirica, E.: XPS study of amorphous zirconium oxide films prepared by sol–gel. Appl. Surf. Sci. **143**, 85–91 (1999)